Numerical and Experimental Investigation of Ice Accretion on a Rotorcraft Engine Air Intake

G. B. Ahn[1], K. Y. Jung[2], and R. S. Myong[3]
Gyeongsang National University, Jinju, Gyeongnam, 660-701, South Korea

H. B. Shin[4]
Korea Aerospace Industries, LTD, Sacheon, Gyeongnam, 664-710, South Korea

and

W. G. Habashi[5]
McGill University, Montreal, QC H3A 2S6, Canada

Ice accretion on the surface of an electro-thermal anti-icing system around a rotorcraft engine air intake was investigated on the basis of computational and experimental methods. A compressible Navier-Stokes-Fourier CFD code was used to determine the fully three-dimensional flow field around the inlet of the engine and the environment control system. Three-dimensional droplet trajectory and ice accretion codes based on the Eulerian approach, DROP3D and ICE3D modules of FENSAP-ICE, were used to calculate the collection efficiency and ice shape on the surface of an engine air intake. Furthermore, an experimental study using an icing wind tunnel was conducted to validate the computational predictions of ice accretion on the surface of the electro-thermal anti-icing system in heat-off and heat-on modes. It is shown that the general shape and range of ice accretion obtained by numerical calculations are in close agreement with experimental observation. In particular, two features of glaze ice formation identified from computational results, the upper parts of intake with the largest ice accretion and the narrow region between these parts showing relatively small ice accumulation, were confirmed in the experimental study.

Part of the paper was presented as Paper 2013-1077 at the 51st AIAA Aerospace Sciences Meeting including the New Horizons Forum and Aerospace Exposition, Grapevine (Dallas/Fr. Worth Region), Texas, 7-10 January 2013.
[1,2] Graduate Student, Department of Aerospace and System Engineering, 501 Jinjudaero.
[3] Professor, Department of Aerospace and System Engineering and Research Center for Aircraft Parts Technology, 501 Jinjudaero. Associate Fellow AIAA. E-mail: myong@gnu.ac.kr (Corresponding Author).
[4] Research Engineer, Research & Development Division, 802 Yucheon-Ri.
[5] Professor, Department of Mechanical Engineering, Montreal, QC H3A 2S6. Fellow AIAA.

Nomenclature

C_D = drag coefficient

C_h = convective heat transfer coefficient

C_{ice} = specific heat at constant pressure for ice (J/kg/K)

C_w = specific heat at constant pressure for water (J/kg/K)

E = total energy of air

Fr = Froude number

$\mathbf{g}$ = non-dimensional gravity vector

h_f = film thickness (m)

k = thermal conductivity of air (W/m/K)

K = droplet inertia parameter

L_{evap} = latent heat of evaporation (J/kg)

L_{fusion} = latent heat of fusion (J/kg)

L_{subl} = latent heat of sublimation (J/kg)

LWC = liquid water content (g/m^3)

$\dot{m}_{evap}$ = instantaneous mass of evaporation (kg/s)

$\dot{m}_{ice}$ = instantaneous mass of ice accretion (kg/s)

$\mathbf{n}$ = unit vector normal to the surface

p = pressure of air

$\boldsymbol{Q}$ = heat flux of air

Q_c = conductive heat transfer

R = gas constant of the air

Re_d = droplet Reynolds number

T = temperature of air

$\tilde{T}$ = temperature at wall/water/ice/air interface (℃)

$\tilde{T}_{d,\infty}$ = droplet temperature at infinity (℃)

T_∞ = air temperature at infinity (°C)

$\tilde{T}_{\infty_0}$ = stagnation temperature at infinity (°C)

t = time (s)

U_∞ = air velocity at infinity (m/s)

$\mathbf{u}_a$ = non-dimensional air velocity vector

$\mathbf{u}_d$ = non-dimensional droplet velocity vector

$\bar{\mathbf{u}}_f$ = mean velocity of the water film (m/s)

$\mathbf{X}$ = position vector

α = non-dimensional water volume fraction

β = collection efficiency

ε = solid emissivity

μ = dynamic viscosity of air (Ns/m^2)

μ_w = dynamic viscosity of water (Ns/m^2)

ρ_a = air density (kg/m^3)

ρ_w = water density (kg/m^3)

σ = Boltzmann constant

$\boldsymbol{\tau}$ = air shear stress tensor (N/m^2)

$\boldsymbol{\tau}_{wall}$ = air wall shear stress tensor (N/m^2)

I. Introduction

ICE accretion on the surface around an engine air intake during all-weather operations can deteriorate the safety of aircraft due to the engine performance degradation [1, 2]. Careful consideration must be given to the issue on how to provide proper ice protection for the aircraft and rotorcraft engine intake [3]. The design of such ice protection systems (IPS), therefore, has remained an important topic in aircraft design and, as a consequence, various methods of ice protection have been developed in the past. They can be classified into two broad categories: de-icing and anti-icing. De-icing methods deal with the intermittent removal, either by mechanical or thermal means, of any ice buildup by destroying the bond between the ice and the adjacent surface. On the other hand, anti-icing methods are

concerned with the prevention, or minimization, of ice buildup on particular surfaces. This is accomplished by either evaporating or by partially evaporating supercooled water droplets that impinge on the surface. Most of the current aircraft utilize thermal energy in the form of hot air or electrical energy in ice protection systems because they have proven to be the most reliable.

Recently, the mechanisms of hot air and electro-thermal systems have been modeled computationally by several researchers. Al-Khalil et al. [4, 5] used a control volume energy analysis to evaluate a hot air anti-icing system for the engine inlet and nacelle. Electro-thermal icing systems have been modeled using finite-difference methods by Keith et al. [6]. Wright et al. [7] and Nishio et al. [8] also studied the combination of anti-icing analysis with ice accretion predictions in order to provide a tool for evaluating the performance of an electro-thermal anti-icing system.

The vital part in the evaluation and design of a proper IPS is the information of collection efficiency on the surface around an engine air intake. It plays a critical role in the anti-icing system sizing, that is, in determining the location of protected areas and how much energy is required to achieve the anti-icing goal. The computational prediction of collection efficiency, ice accretion, and associated performance penalties has been traditionally based on the Lagrangian particle tracking techniques for droplets impingement, such as the NASA LEWICE [9] and ONERA [10, 11] codes, and the inviscid panel or Euler plus boundary layer correction computations for airflow. However, the Lagrangian method is time-consuming, in particular, for three-dimensional calculations and it has a non-negligible difficulty in specifying the droplet seeding locations in complex geometry cases. Moreover, if the compressible Navier-Stokes-Fourier equations are used, one can fully and more directly account for the viscous and heat flux effects required for the ice accretion in computational prediction. For these reasons, and due to its versatility in handling three-dimensional complex geometry like engine intake [12], the CFD-based method [13, 14] was employed in the present work. Specifically, a state-of-the-art icing simulation CFD code, FENSAP-ICE [15-19], was utilized in the investigation of droplet impingement and ice accretion. The computational model employed in the code is based on the compressible Navier-Stokes-Fourier equations and Eulerian droplet impingement method.

The present work was aimed at investigating the range and amount of ice on the surface of an anti-icing system around a rotorcraft engine air intake in heat-off and heat-on modes. Among various types of rotorcraft engine intake, like side mounted static and Pitot dynamic [12], the Pitot type intake utilizing the dynamic pressure in forward flight was considered. In the dry air calculation, a special boundary condition to adjust the pressure at a pressure-outlet

zone of the engine air intake was imposed in order to meet the desired mass flow rate. Then, the ice accretion module utilizing the shear stress and heat flux on the solid wall from air solution and collection efficiency from droplet solution was used in icing simulation. Finally, an experimental investigation using an icing wind tunnel was conducted to validate the computational predictions of ice accretion on the surface of an electro-thermal anti-icing system.

II. Numerical Methods

To simulate the air flow around a rotorcraft engine intake, a compressible Navier-Stokes-Fourier code, FLUENT [20] based on the finite volume method, was used. To predict the droplet impingement and ice accretion on the surface around engine intake, the droplet module (DROP3D) and ice module (ICE3D) of the FENSAP-ICE code [15] were used. The droplet module based on an Eulerian approach augmented by droplet-related continuity and momentum equations solves the fine-grain partial differential equations for droplet velocity and concentration using air flow solution obtained from the air solver. It provides the collection efficiency distributions and impingement limits for droplets over arbitrarily complex bodies or in internal passages. The ice module also solves the fine-grain partial differential equations for ice accretions and yields the three-dimensional shape of ice and the water film thickness on complex three-dimensional surfaces. In the process of ice accretion simulation, aerodynamic grids are first needed to calculate the air flow around the clean shape without ice contamination, and then the collection efficiency is predicted by the droplet solver using the air solutions. Finally, a change in shape due to ice accretion is needed to move the original mesh toward the changed shape. An arbitrary Lagrangian Eulerian (ALE) method that can account for the relative motion of the grid with respect to the fluid is applied during this process. Those procedures are repeated until a user-defined simulation time.

A. Geometric Modeling and Numerical Boundary Conditions

The computational domain consists of an engine intake, nacelle, and the ECS (environment control system). The same grid system generated around the model is applied to the air and droplet solvers. In order to include the interaction between the air intake model and the icing wind tunnel wall, the outside boundaries are treated as a solid surface with no-slip condition. It is expected that a non-negligible effect exists associated with blockage space between the icing wind tunnel wall and the test model.

In this study, a closed type of wind tunnel with dimensions of 2.6m×3.8m×9.9m was considered. Figure 1 shows the overall configuration of an engine intake model used in the wind tunnel test. The solid lines near the engine intake represent the boundary of the heat pad of an electro-thermal anti-icing system. The validity of such boundary will be analyzed by computational and experimental studies. Figure 2 shows the computational grid topology and numerical boundary conditions for the intake model and icing wind tunnel wall. The six hundred thousand tetra-type grids generated by the commercial grid generation tool, GAMBIT [20], were used.

B. Target Mass Flow Rate at Engine Intake

In order to simulate the suction of air flow at the entrance of a rotorcraft engine, a special boundary condition of target mass flow rate was imposed at the end of the computational domain of engine intake. The capability of handling the target mass flow rate was one of the main reasons in choosing the FLUENT code as the air flow solver. In the FLUENT code, a separate menu option to specify the target mass flow rate is provided. The idea was to adjust the pressure at a pressure-outlet zone of the engine air intake in order to meet the desired mass flow rate. That is, the target mass flow rate is achieved by adjusting the pressure value at the pressure-outlet zone up and down at every iteration [20]. This is done on the basis of Bernoulli's equation of the change in pressure, dp, the current and required computed mass flow rates, $\dot{m}, \dot{m}_{req}$, the computed average density at the pressure-outlet boundary, ρ_{ave}, and the area of the pressure-outlet boundary, A, which can be summarized as

$$dp = \frac{\rho_{ave}\left(\dot{m}^2 - \dot{m}_{req}^2\right)}{2\left(\rho_{ave} A\right)^2} \tag{1}$$

The pressure outlet will achieve the converged target mass flow rate unless the flow becomes choked (i.e., the Mach number of the flow in the pressure-outlet zone becomes equal to 1). In passing, it should be noted that the imposing of a target mass flow rate at the end of the engine intake does not change the nature of the pressure-outlet boundary condition and consequently the DROP3D module of the FENSAP-ICE code remains compatible with the FLUENT solutions.

C. Air Flow Solver

The air flow should be computed prior to the simulation of droplet flow fields. The classical compressible Navier-Stokes-Fourier equations were employed as the governing equations. The computational code, FLUENT,

based on the Roe's approximate Riemann solver and the Spalart-Allmaras turbulent model for the Reynolds-averaged Navier-Stokes-Fourier equations was employed to simulate air flow fields.

D. Droplet Solver

The droplet impingement solver is based on an Eulerian approach adopted in the CFD-based methods [16, 21, 22]. It is essentially a two-fluid model (air and water) augmented by droplet-related continuity and momentum equations. The two-phase flow in atmospheric icing can be simulated using a weakly coupled (or one-way coupling) algorithm since the effects of a droplet on the air flow can be ignored. Droplets in liquid water contents, however, are usually found in clouds with a distribution of various droplet diameters instead of droplets of the same size. One such distribution is called the Langmuir D distribution. The resulting impingement limits and intensities may differ for mono-disperse and Langmuir D distributions, but the differences are shown to be small in most of the cases. For this reason, the DROP3D module of the FENSAP-ICE code with mono-disperse assumption was used to simulate droplet impingement on the surface of a rotorcraft engine intake in the present study. In this module, the following partial differential equations of water volume fraction and droplet velocity around the location and time were solved:

$$\frac{\partial \alpha}{\partial t} + \nabla \cdot \left(\alpha \mathbf{u}_d \right) = 0 \tag{2}$$

$$\frac{\partial \mathbf{u}_d}{\partial t} + \mathbf{u}_d \cdot \nabla \mathbf{u}_d = \frac{C_D \, \mathrm{Re}_d}{24K} \left(\mathbf{u}_a - \mathbf{u}_d \right) + \left(1 - \frac{\rho_a}{\rho_w} \right) \frac{1}{Fr^2} \mathbf{g} \tag{3}$$

Note that the equation of droplet velocity (3) is a convection-type equation with no diffusion terms. The term appearing in the right-hand side of the equation (3) represents the source effects which include the aerodynamic drag term described by an empirical drag coefficient for spherical droplets, gravity term, and buoyancy term of the droplet. It should also be mentioned that the effects of the air flow on the droplet solver in the one-way coupling algorithm appear only through this source term. The numerical solutions of equations (2) and (3), in conjunction with the air flow solver, yield water volume fraction and droplet velocity vector everywhere in the computational domain, and the local collection efficiency can be obtained from the following relation:

$$\beta = -\alpha \mathbf{u}_d \cdot \mathbf{n} \tag{4}$$

E. Ice Accretion Solver

Ice accretion is mainly divided into rime ice and glaze ice. In rime ice, the ice tends to form at low ambient temperature, low speed, and low liquid water contents. Therefore, the information of shear stress and heat flux is not needed since the droplet forms ice instantly when droplets impinge on the solid surface. On the other hand, in glaze condition, some portion of droplets remains as water on the surface at warm ambient temperature, high speed, and high liquid water contents. Therefore, the shear stress and heat flux should be considered, meaning that the compressible Navier-Stokes-Fourier code is needed to predict the shear stress and heat flux in an ice accretion solver. The ICE3D module of the FENSAP-ICE code was used to simulate ice accretion on the surface of the rotorcraft engine intake. The physical model of glaze ice accretion employed in the ICE3D module comprises converting the classical algebraic Messinger ice model into a partial differential system of conservation equations of mass balance and heat transfer at the surface:

$$\rho_w \left[\frac{\partial h_f}{\partial t} + \nabla \cdot \left(\bar{\mathbf{u}}_f h_f \right) \right] = U_\infty LWC\beta - \dot{m}_{evap} - \dot{m}_{ice} \tag{5}$$

$$\begin{aligned} \rho_w \left[\frac{\partial \left(h_f C_w \tilde{T} \right)}{\partial t} + \nabla \cdot \left(\bar{\mathbf{u}}_f h_f C_w \tilde{T} \right) \right] &= \left[C_w \tilde{T}_{d,\infty} + \frac{\left| \mathbf{u}_d \right|^2}{2} \right] U_\infty LWC\beta - \frac{\left(L_{evap} + L_{subl} \right)}{2} \dot{m}_{evap} \\ + \left(L_{fusion} - C_{ice} \tilde{T} \right) \dot{m}_{ice} + \varepsilon\sigma \left[\left(T_\infty + 273.15 \right)^4 - \left(T + 273.15 \right)^4 \right] - C_h \left(\tilde{T} - \tilde{T}_{\infty_0} \right) + Q_c \end{aligned} \tag{6}$$

Combined with the following relation obtained by averaging the velocity of the water along the thickness of the film, the equations (5) and (6) will determine three unknowns: $\dot{m}_{ice}$, h_f and $\tilde{T}$

$$\bar{\mathbf{u}}_f \left(\mathbf{X} \right) = \frac{h_f}{2\mu_w} \tau_{wall} \left(\mathbf{X} \right) \tag{7}$$

In this process, the following compatibility conditions are needed:

$$h_f \geq 0,\ \dot{m}_{ice} \geq 0,\ h_f \tilde{T} \geq 0,\ \dot{m}_{ice} \tilde{T} \leq 0 \tag{8}$$

III. Numerical Results

In this study, total four cases with two velocity values (65, 72 m/s) were considered, as summarized in Table 1. An angle of side slip -2 degrees was imposed for the purpose of taking into account the rotor blade downwash effect within the space limitation of wind tunnel test section. The side slip angle was chosen to best match the flow-field obtained by the CFD analysis of the full rotorcraft with blades. The target mass flow rate, which generally varies

depending on engine operation modes, was set 3.8 kg/sec at the end of engine intake in the present study. Figure 3 shows a grid-convergence study using two different grids and it indicates that the numerical solution obtained by using the six hundred thousand grids is in the asymptotic range of convergence. Since the droplet impingement solver, the DROP3D module of the FENSAP-ICE code, was developed on an Eulerian approach sharing the basic grid structure with the air flow CFD solver, the exactly same volumetric grids were used for the FLUENT code and the DROP3D module.

Figures 4 and 5 show the static pressure and velocity distributions in flow field at the cross section of the engine intake and on the frontal surface of the engine intake, respectively. The solid line in Fig. 5 is the boundary of the heat pad of the electro-thermal anti-icing system. The velocity 72 m/s, the sea-level pressure, and the free-stream temperature -10℃ were considered. A high pressure region was formed inside the engine intake while a high velocity region was observed at the outer part of the upper area of engine intake. A stagnation region was found inside the upper circular engine intake lip, implying high probability of ice accretion in the region. Figure 4 also shows a relatively high velocity profile inside the engine intake. This indicates that the suction of air flow at air intake was successfully simulated through a numerical boundary condition of target mass flow rate imposed at the end of the computational domain of engine intake in the FLUENT code. Notice also from Fig. 5 that the general flow field is fully three-dimensional in the case of present rotorcraft engine intake, which is in contrast with the basically axisymmetric nature of flow fields in ordinary commercial transport aircraft engine inlet for small angles of attack [13].

The effects of different droplet size on collection efficiency were analyzed for the mean volume diameters (MVD) from 20 to 40 micrometers. The first case with velocity 72 m/s, temperature -10℃, and LWC 0.3 g/m^3, belonging to intermediate (or more likely rime) ice according to Dickey's data in determining the form of an ice accretion [23], were selected on the basis of the ice condition specified in Appendix C. Collection efficiency distributions on the surface of the electro-thermal anti-icing system are shown in Fig. 6. It can be seen that the size of droplet affects the characteristics of impingement on the solid surface. The case of the MVD 40 micrometer shows a larger area with high collection efficiency than the case of the MVD 20 micrometer. Also, the range of maximum collection efficiency in the case of the MVD 40 micrometer is larger than that of the MVD 20 micrometer. Based on these findings, it may be concluded that the droplet size has a big impact on the ice buildup on the surface

of the air intake. Also, it can be found from the computational results that the boundary of the heat pad of the electro-thermal anti-icing system covers most of the intake surface with non-negligible collection efficiency.

Figure 7 shows an example of ice accretion on the surface of the electro-thermal anti-icing system in heat-off mode. In the second case, the temperature of -20℃, velocity of 72 m/s, LWC of 0.45 g/m^3, MVD of 40 micrometer, and flight time of 15 minutes exposed to the ice conditions were assumed. A single-shot simulation, instead of multi-shot simulation, was used for computational efficiency. The most visible feature in Fig. 7 is the highly non-axisymmetric ice shape and the large ice accretion near the upper parts of intake. In particular, most of the ice accumulated in the region of flow stagnation, which is the inner part of the upper engine intake lip in the present geometry. As expected from the very low temperature -20 ℃, the ice type of numerical simulation was found rime. The figure also shows that most of the ice buildup was confined inside the boundary of the heat pad of the electro-thermal anti-icing system, implying proper identification of the protected region in the low temperature case.

IV. Experimental Investigation and Results

Numerical simulation based on CFD methods is regularly used for droplet catch analysis, ice shape prediction, and subsequent performance degradation analysis. However, there are several challenges in computational simulation like how to accurately model surface roughness and surface water motion and how to reduce ice shape sensitivity to the size of numerical time step. In aircraft icing, icing wind tunnel testing [24, 25] is primarily used to demonstrate the performance of ice protection system for the most critical design cases. Moreover, it is used to provide supporting data that CFD tools used for the analysis are valid for the certification process.

For this reason, an experimental investigation based on icing wind tunnel testing was conducted to validate the computational predictions of ice accretions on the surface of the electro-thermal anti-icing system in heat-off and heat-on modes. The experimental work was performed at the CIRA Icing Wind Tunnel (IWT) [26]. The CIRA IWT is the largest and most advanced icing facility that specializes in experimental research on ice formation. It is considered one of the most modern (open in 2002) facility that can reproduce simultaneously real altitude, temperature, velocity and cloud conditions that are encountered in flight. The CIRA IWT is a closed loop circuit wind tunnel, designed to reproduce realistic flight conditions inside a cold cloud in a controlled and repeatable environment.

A full-scale model of rotorcraft engine intake was manufactured for experimental study. In particular, in order to simulate the air flow entering into the engine intake, an air suction system and associated control units monitoring the correct mass flow rate were installed in the model. The range and general shape of ice accretion were measured by photographic images and cross-sectional drawings. In the third case, an intermediate (or close to glaze) icing condition with a free-stream temperature of -10℃, velocity of 65 m/s, pressure of 84,555 Pa (0.8345 atm), LWC 0.6 g/m^3, MVD 20 micrometer, and flight time of 30 minutes under icing condition was considered. Figure 8 shows the computational prediction of collection efficiency on the surface of the anti-icing system in a relatively high LWC case with 0.6 g/m^3. Similar to a relatively low LWC case with 0.3 g/m^3, as shown in Fig. 6, regions with high collection efficiency were found at the inner part of the upper and side lips of engine intake and were confined inside the boundary of the heat pad of the electro-thermal anti-icing system. However, the width of the half-circle shape with a high collection efficiency of the present lower speed case (65 m/s) was found smaller than that of the higher speed case (72 m/s). In addition, the highest collection efficiency was predicted at the inner part of the upper lip of engine intake.

Figure 9 shows the comparison of computational prediction and experimental image data of ice accretion in the intermediate icing condition with a relatively warm free-stream temperature of -10℃. According to Dickey's data on ice shape types as function of speed and ambient temperature, the present case with speed 65 m/s (126 Knot) and temperature 263 K (14 F) for the condition LWC 0.6 g/m^3 and MVD 20 μm belongs to the intermediate (or close to glaze) ice. In the computational calculation, a single-shot simulation was used for computational efficiency. In general, it can be seen that the range and general shape of ice accretion are in close agreement with experimental observation. In particular, two features of intermediate (or close to glaze) ice formation identified from computational results, the upper parts of intake with the largest ice accretion and narrow region between these parts showing relatively small ice accumulation, are clearly confirmed in experimental results. Also, when compared with the ice accretion in pure rime icing condition with a low temperature of -20 ℃ shown in Fig. 7, there exist notable differences; 1) intermediate (or close to glaze) ice formation is more pronounced at the upper parts of intake than at other parts; 2) rime ice formation is in general found in more broad region and in more uniform manner. Furthermore, the location of two features of intermediate (or close to glaze) ice formation matches precisely with experimental observation. From these findings, it may be concluded that the CFD-based simulation method can provide the preliminary information of the range (location of protected area) and general shape of ice accretion on

the surface around an engine air intake. In passing, slight asymmetry observed from both the simulation and experiment is due to the asymmetric flow condition, an angle of side slip -2 degrees, imposed for the purpose of simulating the rotor blade downwash effect.

Figure 10 shows the comparison of computational and experimental ice shapes at the central cross section of the upper lip of engine intake, the exact location of which is indicated in Fig. 9. The cross-sectional shape of ice accretion was measured by hand drawing during the icing wind tunnel test. The comparison of ice shapes clearly shows that computational results are in qualitative agreement with the experimental data. In particular, the existence of two peaks at the inner part of the air intake lip and a region with relatively small flat ice accumulation between these peaks was clearly found in both computational and experimental results. This irregular ice shape can be considered proof of intermediate (or close to glaze) ice formation. In addition, the thickness of ice accretion predicted is in close agreement with experimental observation.

Finally, in order to evaluate the performance of the electro-thermal anti-icing system in heat-on mode and to validate the associated computational prediction, the fourth case, a relatively low temperature case, V = 72 m/s, P = 101,325 Pa, T = 255 K, LWC = 0.3 g/m^3, MVD = 20 μm, was investigated. Figure 11 shows the comparison of computational prediction and experimental image data of ice accretion in the heated case. Almost negligible ice accretion of the order of a few millimeters was predicted on the surface of the electro-thermal anti-icing system in numerical simulation and such behavior was confirmed in experimental image data. It may again imply the proper design of the boundary of the heat pad of the electro-thermal anti-icing system.

V. Conclusions

In this study, numerical and experimental investigation of ice accretion on the surface of the anti-icing system around a Pitot dynamic type rotorcraft air intake was performed. The state-of-the-art air flow, droplet trajectory, and ice accretion codes based on the Eulerian approach were used to predict the collection efficiency and ice shape on the surface of the anti-icing system. In order to meet the target mass flow rate at the entrance of a rotorcraft engine, a special numerical boundary condition based on the Bernoulli's equation was imposed at the end of the computational domain of engine intake.

It was shown from numerical simulations that the size of water droplet has a big impact on the impingement limits and maximum collection efficiency, being greater for larger droplets. In addition, experimental investigation

using an icing wind tunnel was conducted to validate the computational predictions of ice accretions on the surface of the anti-icing system around the air intake. The comparison with icing wind tunnel test data of ice accretion in heat-off and heat-on modes showed that the general shape and range of ice accretion obtained by numerical calculations are in close agreement with experimental observation. In particular, two features of intermediate (or close to glaze) ice formation in heat-off mode, the upper parts of intake with the largest ice accretion and narrow region between these parts showing relatively small ice accumulation, were clearly confirmed in experimental results. Furthermore, the location of such features was found to match precisely with experimental observation, demonstrating the capability of the present CFD-based icing simulation method for fully three-dimensional complex geometry like the rotorcraft engine air intake.

Acknowledgments

This work was supported by Korea Aerospace Industries Ltd. and partially supported by the National Research Foundation of Korea funded by the Ministry of Education, Science and Technology (NRF 2009-009414, NRF 2012-R1A1A4A01-010242), South Korea. The authors thank the referees of this paper for their valuable and very helpful comments.

References

[1] Kind, R. J., Potapczuk, M. G., Feo, A., Golia, C., and Shah, A. D., "Experimental and Computational Simulation of In-Flight Icing Phenomena," *Progress in Aerospace Sciences*, Vol. 34, 1998, pp. 257-345.

[2] Gent, R. W., Dart, N. P., and Cansdale, J. T., "Aircraft Icing," *Philosophical Transactions of the Royal Society A*, Vol. 358, 2000, pp. 2873-2911.

[3] Cao, Y., and Chen, K., "Helicopter Icing," *The Aeronautical Journal*, Vol. 114, No. 1152, 2010, pp. 83-90.

[4] Al-Khalil, K. M., Keith, T. G., Jr., De Witt, K. J., Nathman, J. K., and Dietrich, D. A., "Thermal Analysis of Engine Inlet Anti-Icing Systems," *Journal of Propulsion and Power*, Vol. 6, No. 5, 1990, pp. 628-634.

[5] Al-Khalil, K. M., Keith, T. G., and DeWitt, K. J., "Icing Calculations on a Typical Commercial Jet Engine Inlet Nacelle," *Journal of Aircraft*, Vol. 34, No. 1, 1997, pp. 87-93.

[6] Keith, T. G., De Witt, K. J., Wright, W. B., and Masiulaniec, K. C., "Overview of Numerical Codes Developed for Predicted Electrothermal De-Icing of Aircraft Blades," *AIAA Paper 88-0288*, 1988.

[7] Wright, W. B., Keith, T. G., and De Witt, K. J., "Numerical Simulation of Icing, Deicing, and Shedding," *AIAA Paper 91-0665*, 1991.

[8] Nishio, S., and Kato, S., "Development of Ice Accretion and Anti-Icing System Simulation Code," *ICAS 2004-7.5.R.2, 24th International Congress of the Aeronautical Sciences*, 2004.

[9] Ruff, G. A., and Berkowitz, B. M., "Users' Manual for the NASA Lewis Ice Accretion Prediction Code (LEWICE)," *NASA-TR-185129*, 1990.

[10] Hedde, T., and Guffond, D., "ONERA Three-Dimensional Icing Model," *AIAA Journal*, Vol. 33, No. 6, 1995, pp. 1038-1045.

[11] Wright, W. B., Gent, R. W., and Guffond, D., "DRA/NASA/ ONERA Collaboration on Icing Research, Part II. Prediction of Airfoil Ice Accretion," *NASA CR-202349*, 1997.

[12] Heise, R., *Implementation of a Two-Stream-Fan in the CIRSTEL System*, Ph.D. Thesis, University of Stellenbosch, South Africa, 2006.

[13] Shen, X. B., Lin, G. P., Yu, J., Bu, X. Q., and Du, C. H., "Three-Dimensional Numerical Simulation of Ice Accretion at the Engine Inlet," *Journal of Aircraft*, Vol. 50, No. 2, 2013, pp. 635-642.

[14] Jung, S. K., and Myong, R. S., "A Second-Order Positivity-Preserving Finite Volume Upwind Scheme for Air-Mixed Droplet Flow in Atmospheric Icing," *Computers & Fluids*, Vol. 86, 2013, pp. 459-469.

[15] *FENSAP-ICE Software Package Version 2008*, Newmerical Technologies Inc., Montreal, 2008.

[16] Bourgault., Y., Boutanios, Z., and Habashi, W. G., "Three-Dimensional Eulerian Approach to Droplet Impingement Simulation Using FENSAP-ICE, Part 1: Model, Algorithm, and Validation," *Journal of Aircraft*, Vol. 37, No. 1, 2000, pp. 95-103.

[17] Nakakita, K., Nadarajah, S., and Habashi, W. G., "Toward Real-Time Aero-Icing Simulation of Complete Aircraft via FENSAP-ICE," *Journal of Aircraft*, Vol. 47, No. 1, 2010, pp. 96-109.

[18] Aliaga, C. N., Aubé, M. S., Baruzzi, G. S., and Habashi, W. G., "FENSAP-ICE-Unsteady: Unified In-Flight Icing Simulation Methodology for Aircraft, Rotorcraft, and Jet Engines," *Journal of Aircraft*, Vol. 48, No. 1, 2011, pp. 119-126.

[19] Reid, T., Baruzzi, G. S., and Habashi, W. G., "FENSAP-ICE: Unsteady Conjugate Heat Transfer Simulation of Electrothermal De-Icing," *Journal of Aircraft*, Vol. 49, No. 4, 2012, pp. 1101-1109.

[20] *ANSYS FLUENT Software Package Version 12.0*, ANSYS Inc., Canonsburg, PA, 2009.

[21] Durst, F., Milojevic, M., and Schonung, B., "Eulerian and Lagrangian Predictions of Particulate Two-Phase Flows: A Numerical Study," *Applied Mathematical Modelling*, Vol. 8, No. 2, 1984, pp. 101-115.

[22] Scott, J., Hankey, W., Giessler, F., and Gielda, T., "Navier–Stokes Solution to the Flow Field over Ice Accretion Shapes," *Journal of Aircraft*, Vol. 25, No. 8, 1988, pp. 710-716.

[23] Dickey, T. A., "An Analysis of the Effects of Certain Variables in Determining the Form of an Ice Accretion," *AEL 1206*, Aeronautical Engineering Laboratory, Naval Air Experimental Station, Philadelphia, U.S., 1952.

[24] Tezok, F., and Fritz, E., "Icing Tunnel Testing Methodology: Pre-Test CFD, Tunnel Peculiarities, Scaling Effects," *Proceedings of the Aerodynamics Symposium*, CASI (Canadian Aeronautics and Space Institute), Ottawa, Canada, Vol. 6, 1997, pp. 81-100.

[25] Papadakis, M., Hung, K. E., Vu, G. T., Yeong, H. W., Bidwell, C. S., Breer, M. D., and Bencic, T. J., "Experimental Investigation of Water Droplet Impingement on Airfoils, Finite Wings, and an S-Duct Engine Inlet," *NASA TM-2002-211700*, 2002.

[26] Vecchione, L., De Matteis, P. P., and Leone, G., "An Overview of the CIRA Icing Wind Tunnel," *AIAA Paper 2003-900*, 2003.

	Velocity (m/s)	Temperature (K)	LWC (g/m^3)	MVD (μm)
Case I	72	263	0.3	20, 30, 40
Case II	72	253	0.45	40
Case III	65	263	0.6	20
Case IV	72	255	0.3	20

Table 1 Icing conditions (sea level).

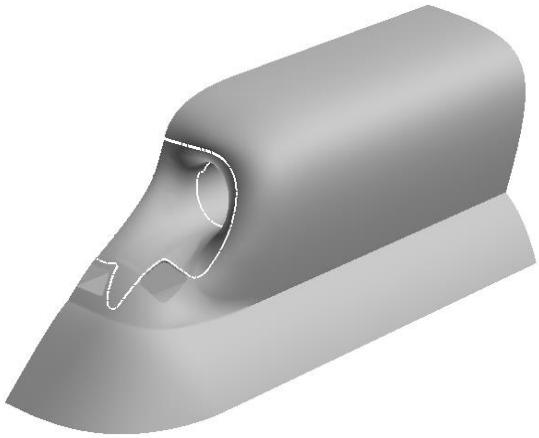

Fig. 1 Engine air intake model configuration.

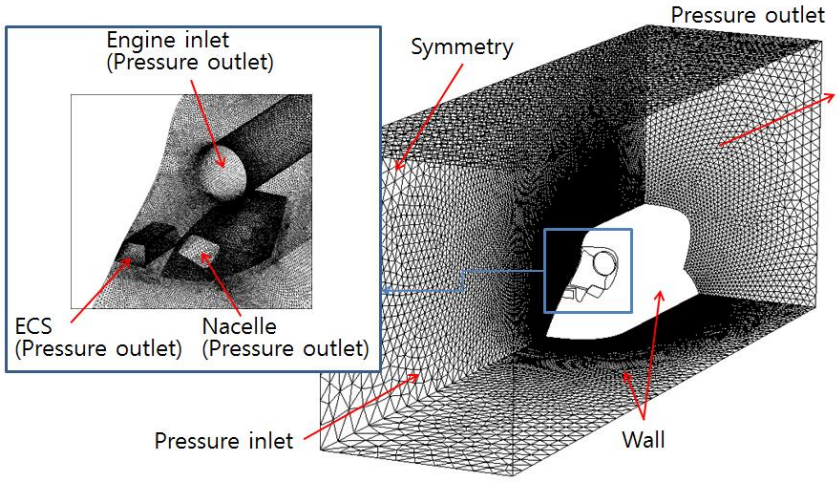

Fig. 2 Computational grid topology and boundary conditions for the intake model and icing wind tunnel (2.6m×3.8m×9.9m).

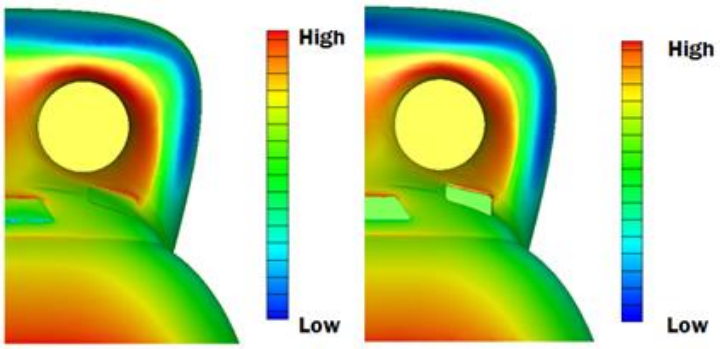

Fig. 3 Pressure distribution around the engine air intake for different grids (left: 200,000, right: 600,000).

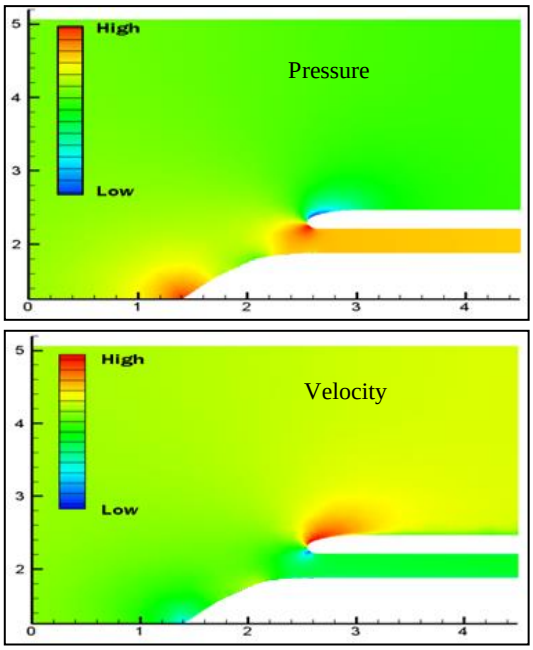

Fig. 4 Pressure and velocity distributions in flow field around the engine air intake (side view); V = 72 m/s, P = 101,325 Pa, T = 263 K.

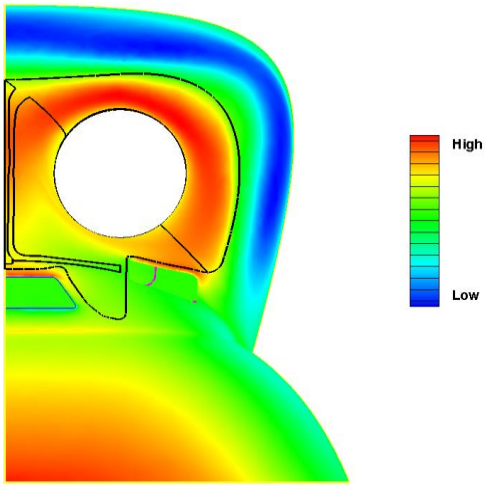

Fig. 5 Pressure distributions around the engine air intake (frontal view); V = 72 m/s, P = 101,325 Pa, T = 263 K.

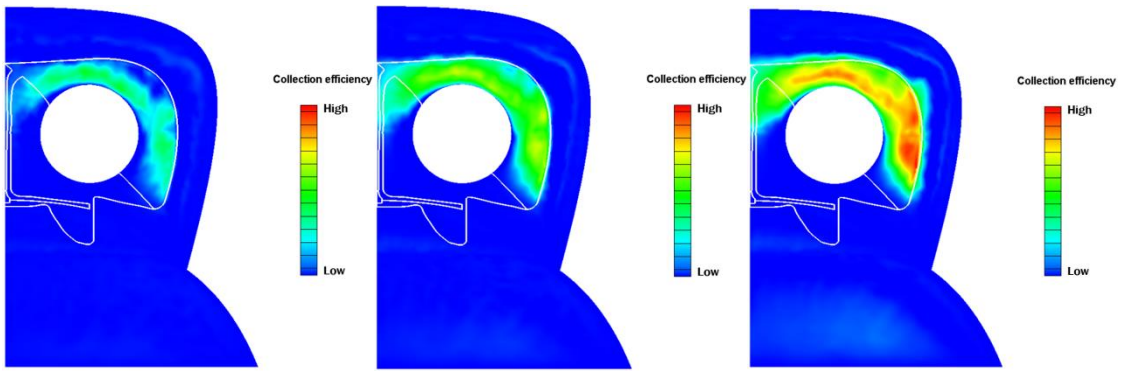

Fig. 6 Collection efficiency distributions on the surface of an electro-thermal anti-icing system (case I); V = 72 m/s, P = 101,325 Pa, T = 263 K, LWC = 0.30 g/m^3, MVD = 20, 30, 40 μm.

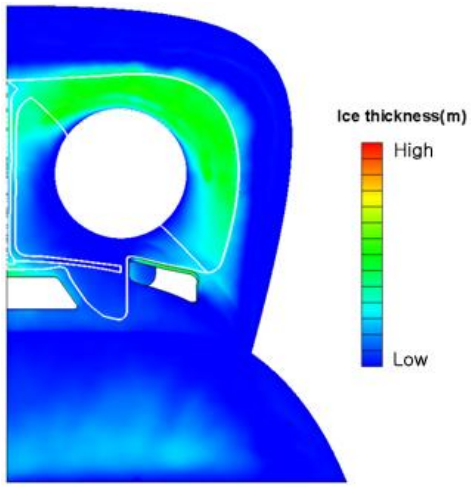

Fig. 7 Ice accretion on the surface of an electro-thermal anti-icing system (case II); V = 72 m/s, P = 101,325 Pa, T = 253 K, LWC = 0.45 g/m^3, MVD = 40 μm, time = 15 mins.

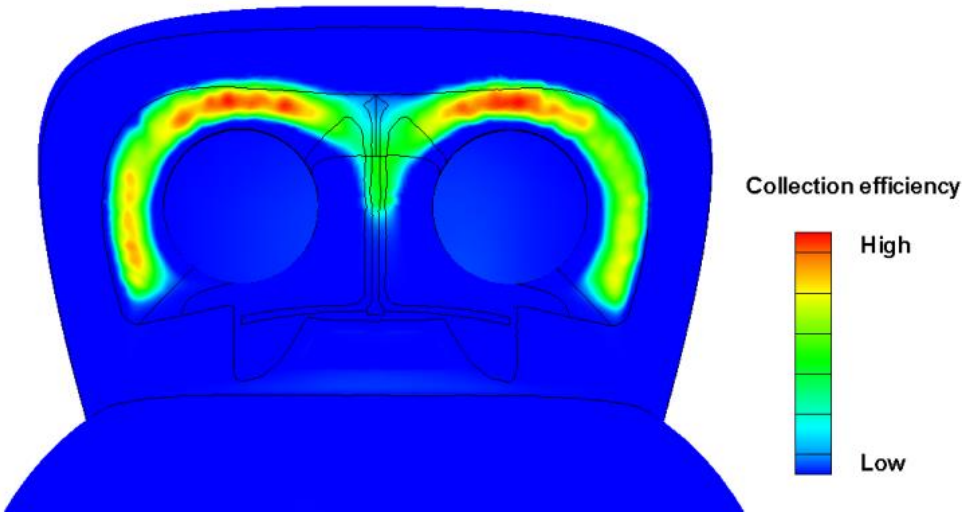

Fig. 8 Prediction of collection efficiency on the surface of an electro-thermal anti-icing system (case III); V = 65 m/s, P = 84,555 Pa, T = 263 K, LWC = 0.6 g/m^3, MVD = 20 μm.

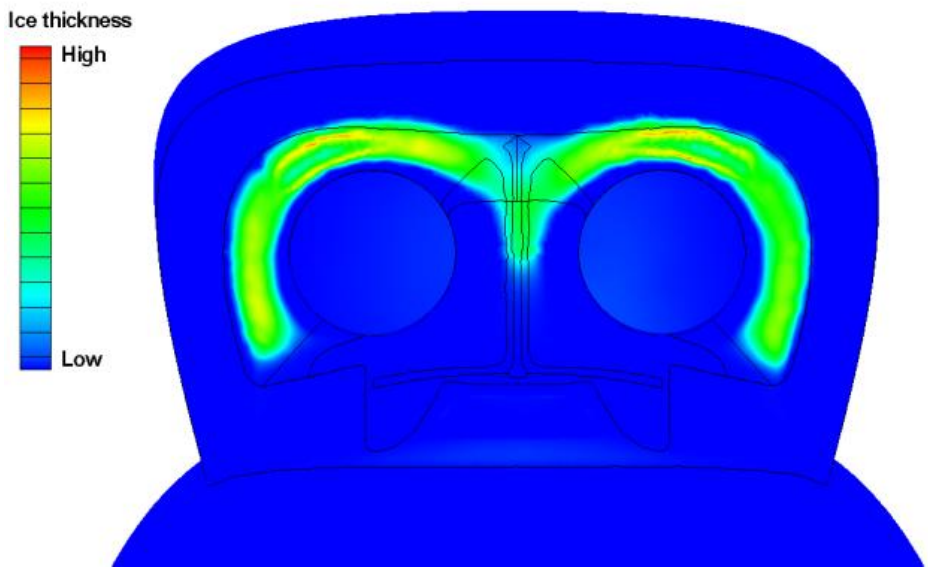

Fig. 9 Comparison of computational prediction and experimental image data of ice accretion (case III);

V = 65 m/s, P = 84,555 Pa, T = 263 K, LWC = 0.6 g/m^3, MVD = 20 μm, time = 30 mins.

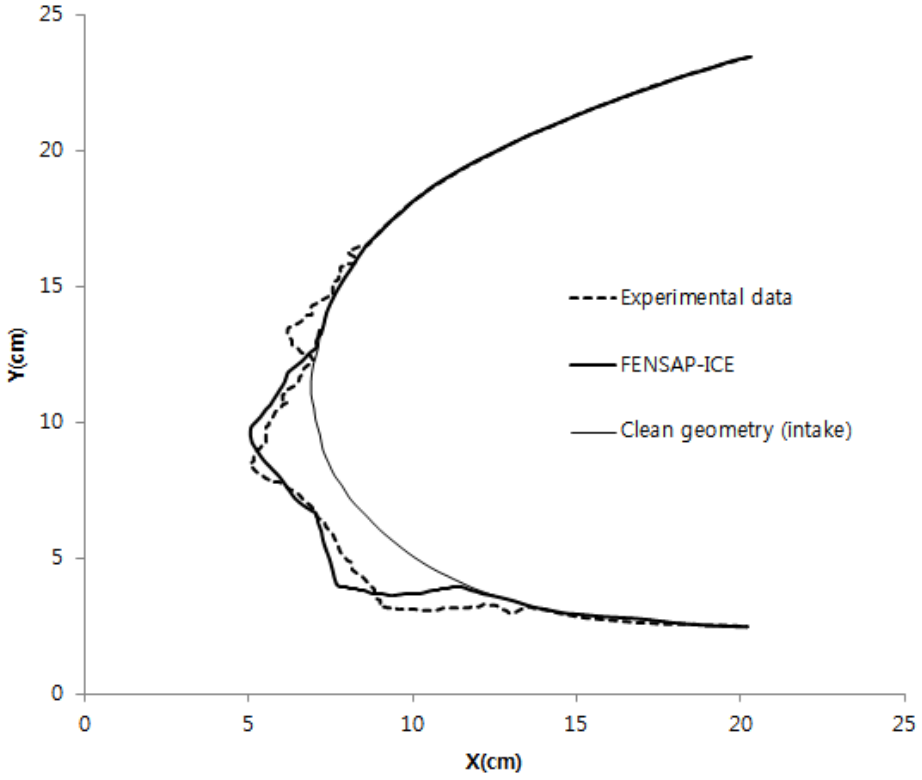

Fig. 10 Comparison of cross-sectional ice shapes (case III); V = 65 m/s, P = 84,555 Pa, T = 263 K, LWC = 0.6 g/m^3, MVD = 20 μm, time = 30 mins.

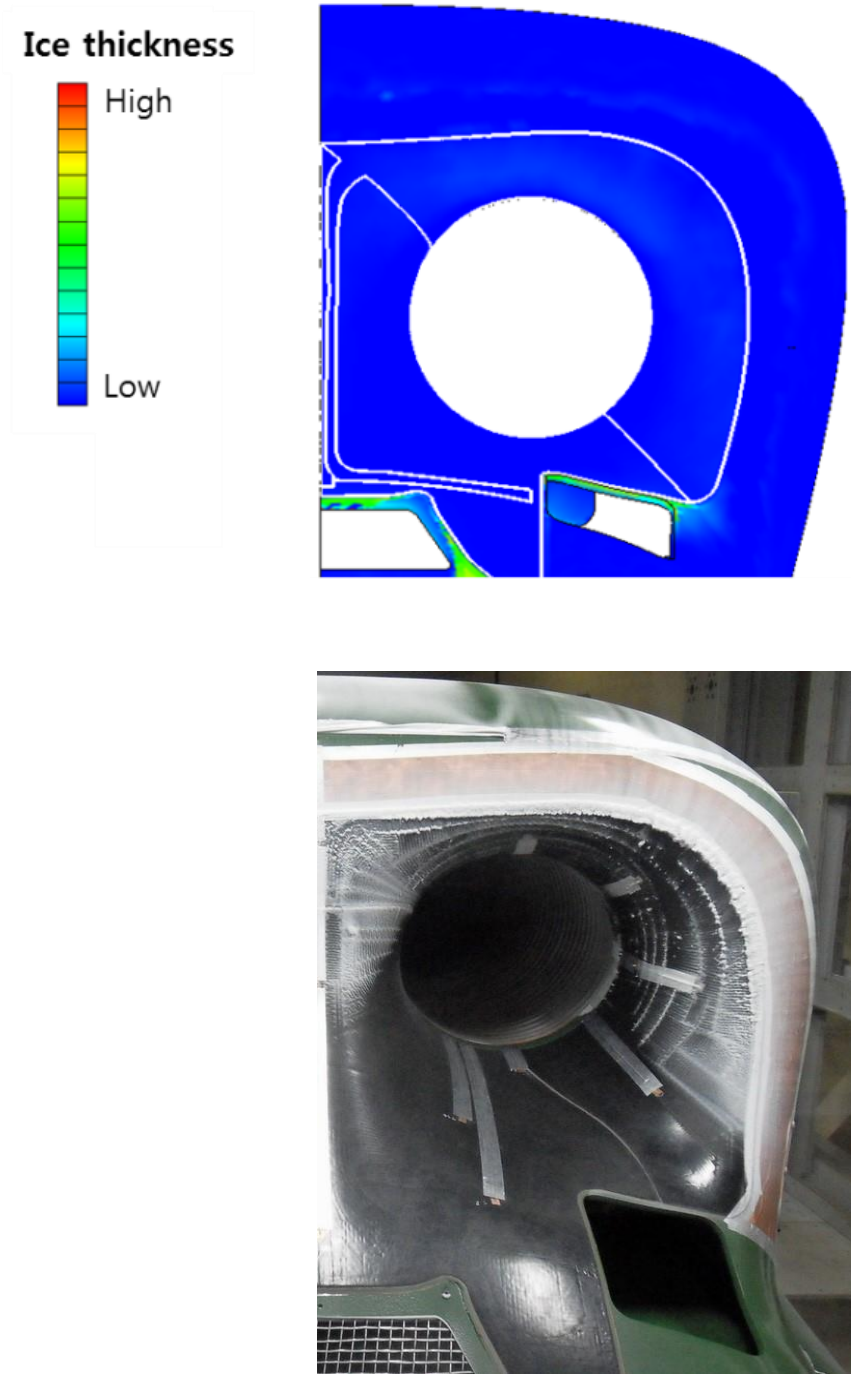

Fig. 11 Comparison of computational prediction and experimental image data of ice accretion in a heated case (case IV); V = 72 m/s, P = 101,325 Pa, T = 255 K, LWC = 0.3 g/m^3, MVD = 20 μm.